Magnetron sputtered Al co-doped with Zr-Fe_2O_3 photoanode with fortuitous Al_2O_3 passivation layer for lowering the onset potential for PEC solar water splitting

Tae Sik Koh[1,†], Periyasamy Anushkkaran[1,†], Jun Beom Hwang[1], Sun Hee Choi[2], Weon-Sik Chae[3], Hyun Hwi Lee[2,*] and Jum Suk Jang[1,*]

[1] Division of Biotechnology, College of Environmental and Bioresource Sciences, Jeonbuk National University, Iksan, 54596, Republic of Korea

[2] Pohang Accelerator Laboratory, POSTECH, Pohang 37673, Korea.

[3] Daegu Center, Korea Basic Science Institute, Daegu 41566, Republic of Korea.

*Correspondence: hhleec@postech.ac.kr (H.H.L.); jangjs75@jbnu.ac.kr (J.S.J.)

† These authors contribute equally.

1.1. Characterization

In order to examine the purity and crystallinity of as-synthesized photoanode samples, synchrotron X-ray diffraction (SR-XRD) measurements were conducted at BL5A beamline of PLS-II (Pohang Light Source II) in Korea. The local structure of Fe in *x*:Al-Zr/HT photoanodes was investigated by Extended x-ray absorption fine structure (EXAFS) spectroscopy. Fluorescence spectra for Fe K-edge (E_0=7,112 eV) were taken at BL7D beamline of PLS-II in Korea. The obtained data were background-removed, normalized and Fourier-transformed. The morphology of all samples was observed using high resolution field-emission scanning electron microscopy (HR-FESEM, Hitachi SU8230, Korean Basic Science Institute) and high-resolution transmission electron microscopy (HR-TEM, Center for University-wide Research Facilities (CURF) at Jeonbuk National University) observations were carried out. X-ray photoelectron spectroscopy (XPS) measurement were performed on a PHI Quantera II spectrometer using a monochromatic AlKα X-ray source (Kongju National University) and the binding energy was calibrated by the adventitious carbon peak of C 1s at 284.8 eV. The optical properties of the as-prepared photoanodes were evaluated by ultraviolet-visible absorption spectra using a UV-Vis spectrophotometer (UV-2600, Shimadzu). The band gap energy of the photoanode was determined from an indirect transition of the Tauc method [1]:

$$(\alpha h\upsilon)^{1/n} = A(h\upsilon - E_g) \quad \text{(S1)}$$

where, α is the absorption coefficient, h is Planck's constant, υ is the photon frequency, A is a proportionality constant, E_g is the optical bandgap, and n is an exponent that depends on the nature of the electronic transitions. Since hematite is an indirect bandgap semiconductor, the value of n is 2.

1.2. Photoelectrochemical (PEC) measurements

PEC measurements were performed with an Ivium CompactStat potentiostat (Ivium Instruments, The Netherlands) in a three-electrode electrochemical cell using the prepared α-Fe_2O_3 as the working electrode, Pt wire as the counter electrode and Hg/HgO as the reference electrode. An aqueous solution of 1 M NaOH (pH = 13.6) was used as the electrolyte. Current density-potential characteristics were measured by an Ivium CompactStat potentiostat with illumination using a solar simulator with the standard global solar light (AM 1.5G, 100 mW cm^{-2}). The potential was calculated against the reversible hydrogen electrode (RHE) by using the following Nernst equation:

$$E_{\mathrm{RHE}} = E_{\mathrm{Hg/HgO}} + 0.059\mathrm{pH} + E^{0}_{\mathrm{Hg/HgO}} \quad \text{(S2)}$$

($E^{0}_{\mathrm{Hg/HgO}} = 0.095$ V at 25 ^{0}C)

Current density-Potential curves were obtained from 0.3 to 1.7 V vs. RHE with a scan rate of 50 mV s^{-1}. The Nyquist plots calculated from electrochemical impedance spectroscopy (EIS) were measured over the frequency range from 3000 kHz to 0.5 Hz under a 1-sun illumination condition. The Mott-Schottky plots were measured in dark condition at a frequency of 100 Hz to understand the donor density (N_D) and flat band potential based on the following equation [2]:

$$1/C^2 = \frac{2}{q\varepsilon\varepsilon_0 N_D A^2}(V - E_{FB} - k_B T/q) \quad \text{(S3)}$$

where, q is the electron charge (1.602×10^{-19} C), ε is the dielectric constant of hematite (80), ε_0 is the permittivity of vacuum (8.854×10^{-12} F m^{-1}), E_{FB} is the flat band potential, k_B is the Boltzmann constant (1.38×10^{-23} J K^{-1}), T is the temperature and C is the capacitance derived from the electrochemical impedance obtained at each potential (V). The intensity modulated photocurrent spectroscopy (IMPS) study was performed using a blue LED by a frequency-response analyzer with the peak wavelength of 520 nm. The bulk charge separation efficiency (η_{bulk}) and surface charge separation efficiency ($\eta_{surface}$) of as-synthesized photoanodes were measured by the addition of 0.5 M H_2O_2 in 1 M NaOH electrolyte solution. The photocurrent density in the presence of H_2O_2 could represent the number of separated charges that successfully reach the electrode surface without recombination in the bulk, since H_2O_2 has a faster oxidation rate and a lower overpotential than that of H_2O. The η_{bulk} and $\eta_{surface}$ were calculated by following equations [3]:

$$J_{H_2O} = J_{abs} \times \eta_{bulk} \times \eta_{surface} \quad \text{(S4)}$$

$$J_{H_2O_2} = J_{abs} \times \eta_{bulk} \quad \text{(S5)}$$

$$\eta_{bulk} = J_{H_2O_2}/J_{abs} \times 100 \quad \text{(S6)}$$

$$\eta_{surface} = J_{H_2O}/J_{H_2O_2} \times 100 \quad \text{(S7)}$$

where, J_{H2O} is the measured photocurrent density, J_{abs} is the photon absorption expressed as a current density (i.e., absorbed photon-to-current efficiency APCE =100%), and J_{H2O2} is the photocurrent density in the presence of H_2O_2.

Table S1. Comparative photocurrents density results of hematite photoanodes at 1.23 V vs. RHE with previous studies.

Photoanode Materials	Photocurrent without surface modification ($mA\ cm^{-2}$ at 1.23 V_{RHE})	Photocurrent after surface modification ($mA\ cm^{-2}$ at 1.23 V_{RHE})	Ref.
Al-Fe_2O_3	1.00	-	[4]
FeNiOOH-FeF_x/Zr-Fe_2O_3	1.69	2.81	[5]
Zr-Fe_2O_3/NiFe MOF	1.41	2.19	[6]
F-FeOOH/Zr-Fe_2O_3	1.65	2.11	[7]
CoPi:(F,Zr)-Fe_2O_3	1.91	2.29	[8]
(Ti,Zr)-Fe_2O_3	1.51	-	[9]
(Zr,Sn)-Fe_2O_3	1.64	-	[10]
CoPi:(Ti,Al)-Fe_2O_3	1.32	1.60	[11]
(F,Ti)-Fe_2O_3	1.61	-	[12]
(Ti,Zn)-Fe_2O_3	1.02	-	[13]
CoPi:Al/Zr-Fe_2O_3	**1.85**	**1.98**	**This work**

Table S2. Electrochemical impedance spectroscopy (EIS) fitting parameters at 1.0 V vs. RHE for Zr/HT, 2:Al-Zr/HT, 6:Al-Zr/HT and 10:Al-Zr/HT photoanodes.

Samples	R_S (Ω)	R_1 (Ω)	CPE_1 (μF)	R_2 (Ω)	CPE_2 (μF)
Zr/HT	36.24	41.28	41.88	137.8	899.2
2:Al-Zr/HT	20.5	61.74	46.51	68.29	1089
6:Al-Zr/HT	21.4	67.01	31.50	68.31	837.4
10:Al-Zr/HT	32.94	57.06	37.30	80.97	1105

Table S3. PL lifetime parameters of the examined Zr/HT, 2:Al-Zr/HT, 6:Al-Zr/HT and 10:Al-Zr/HT photoanodes.

Samples	A_1 (%)	τ_1 (ns)	A_2 (%)	τ_2 (ns)	A_3 (%)	τ_3 (ns)	$<\tau>$[a)] (ns)
Zr/HT	67.5	0.05	31.4	0.28	1.1	2.9	0.77
2:Al-Zr/HT	69.9	0.05	29.8	0.24	0.3	3.7	0.53
6:Al-Zr/HT	61.5	0.05	37.7	0.27	0.8	2.5	0.51
10:Al-Zr/HT	60.8	0.06	38.0	0.29	1.2	2.1	0.51

The time-resolved PL intensity is defined by $I(t) = \sum A_i e^{-t/\tau_i}$, where *I(t)* is the PL intensity as a function of time, *A* is the amplitude, τ is the PL lifetime, and *i* is the subcomponent number of lifetime [14-16] [a)] The intensity-weighted average lifetime is calculated by the following equation: $<\tau>= \sum_i A_i\tau_i^2 / \sum_i A_i\tau_i$.

Table S4. Frequency at the minimum imaginary component (f_{min}) and average electron transport time in the IMPS spectra for Zr/HT, 2:Al-Zr/HT, 6:Al-Zr/HT and 10:Al-Zr/HT photoanodes.

Samples	f_{min} (Hz)	Electron transport time (μs)
Zr/HT	316.0	504
2:Al-Zr/HT	595.7	267
6:Al-Zr/HT	188.4	845
10:Al-Zr/HT	251.2	634

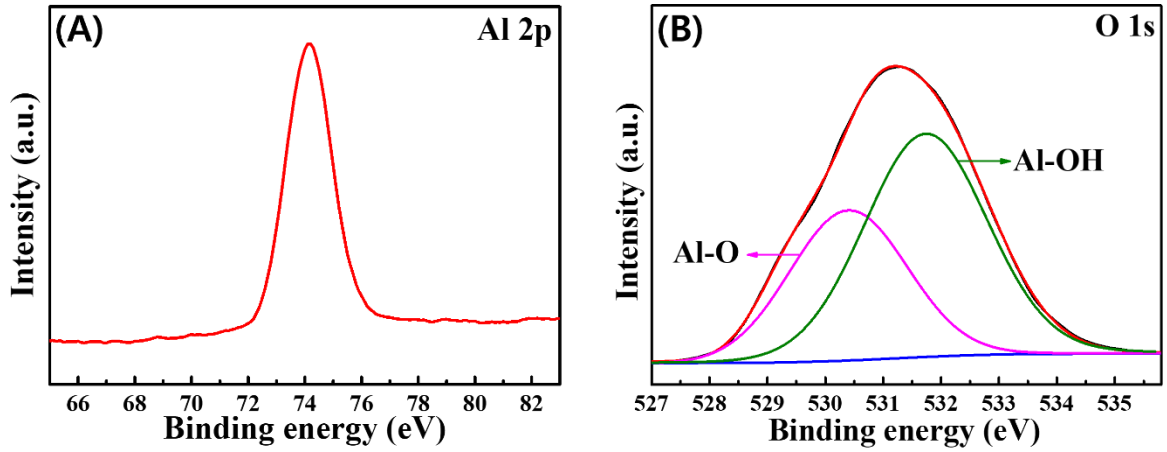

Figure S1. The XPS spectra of (A) Al 2p and (B) O 1s for 2nm Al/Zr-FeOOH.

As can be seen from Figure S1A, the binding energies of Al 2p peak positioned at 74.1 eV corresponds to Al_2O_3 composition [17]. The O 1s peak is deconvoluted into two major peaks: one at 531.7 eV, consistent to Al–OH bonds and the other at 530.4 eV associated with Al–O bonds peak [18,19].

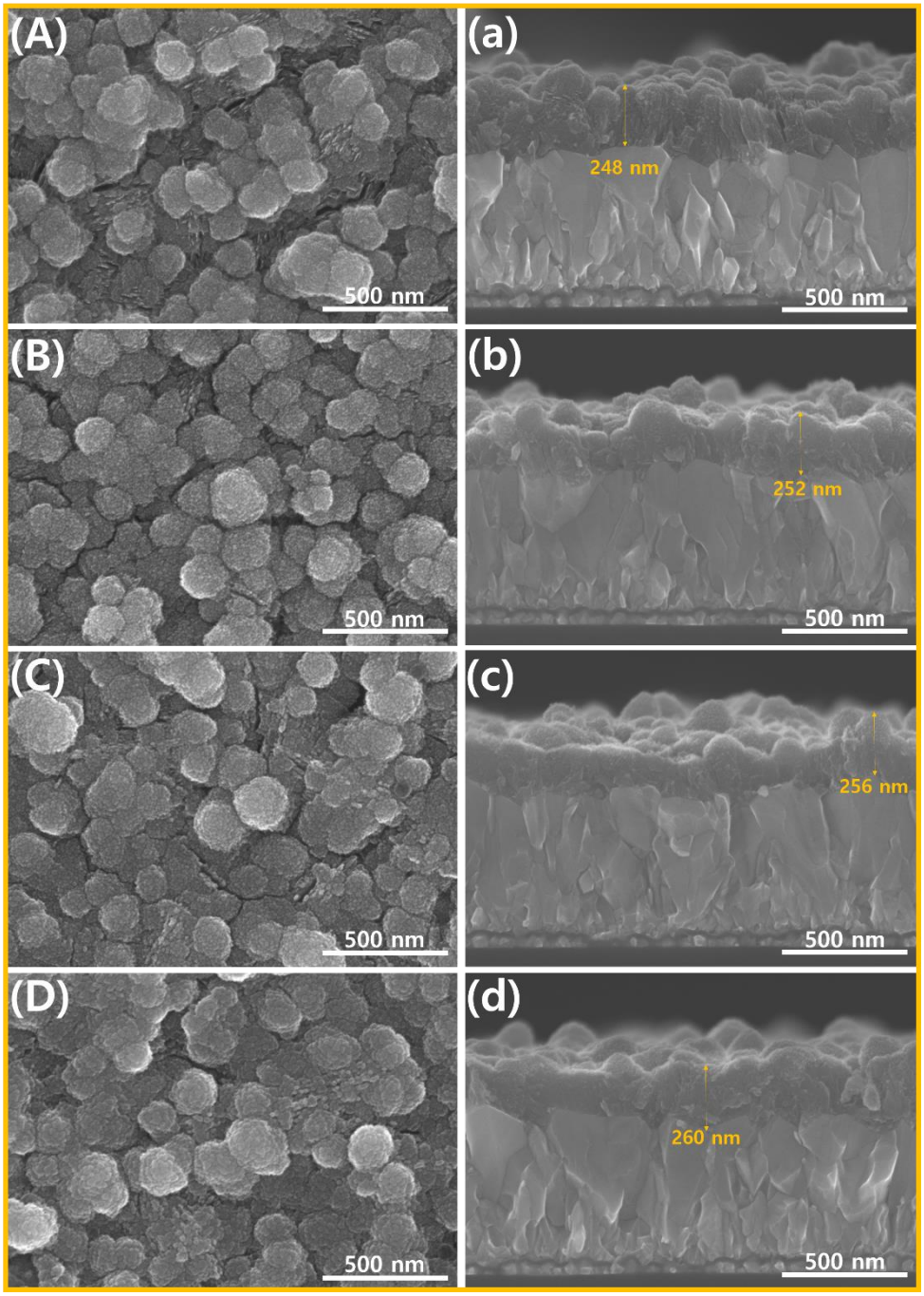

Figure S2. FESEM image (top and cross-sectional view) of Al deposited photoanode before quenching. (A,a) Zr-FeOOH, (B,b) 2nm Al/Zr-FeOOH, (C,c) 6nm Al/Zr-FeOOH, (D,d) 10nm Al/Zr-FeOOH.

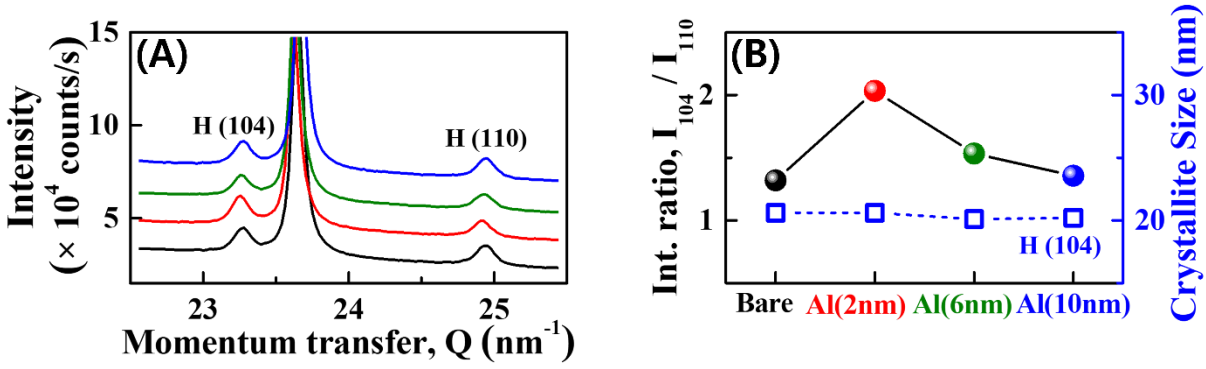

Figure S3. (A) Diffraction profiles near the two major H(104) and H(110) peaks. (B) Integrated intensity ratio (solid circles) of H(104) *vs*. H(110) peak and the crystallite size (dashed blue squares) calculated from the H(104) peak.

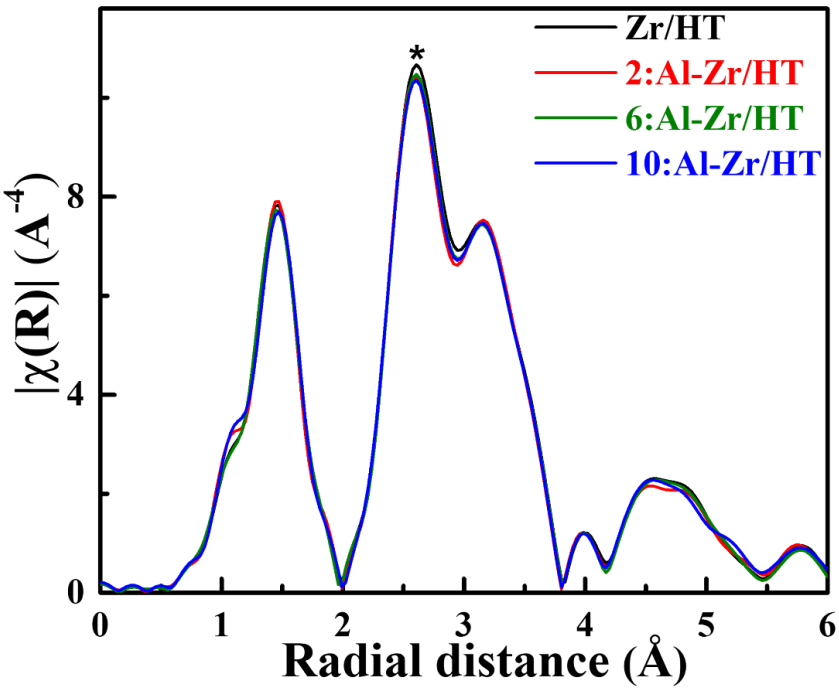

Figure S4. Fourier-transformed spectra of k^3-weighted EXAFS functions for the Fe K-edges of *x*:Al-Zr/HT photoanodes.

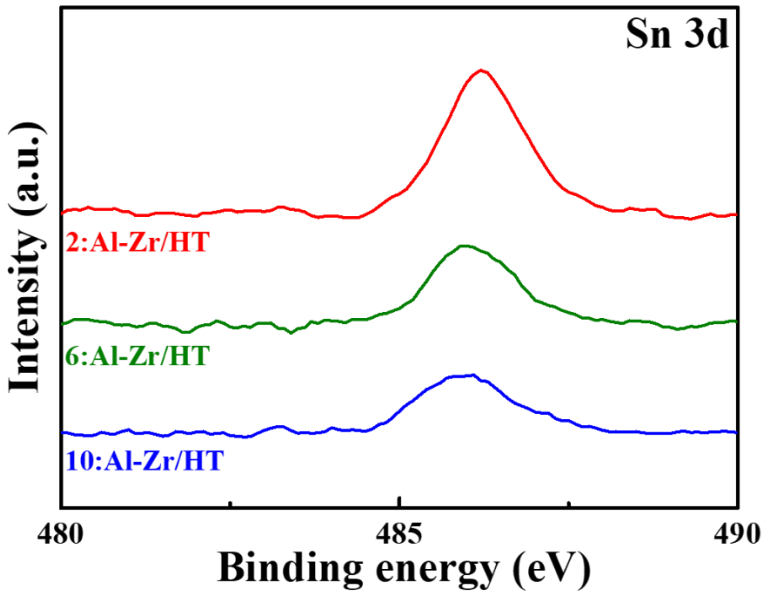

Figure S5. XPS narrow scan spectra of Sn 3d *x*:Al-Zr/HT photoanodes.

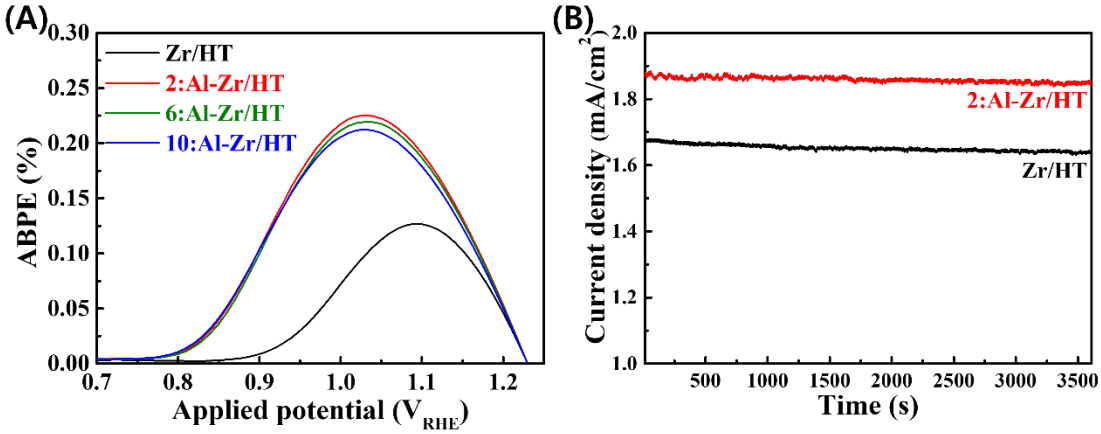

Figure S6. (A) ABPE as a function of applied potential for Zr/HT and x:Al-Zr/HT photoanodes and (B) long-term stability at 1.23 V *vs.* RHE using 1 M NaOH electrolyte for Zr/HT and x:Al-Zr/HT photoanodes.

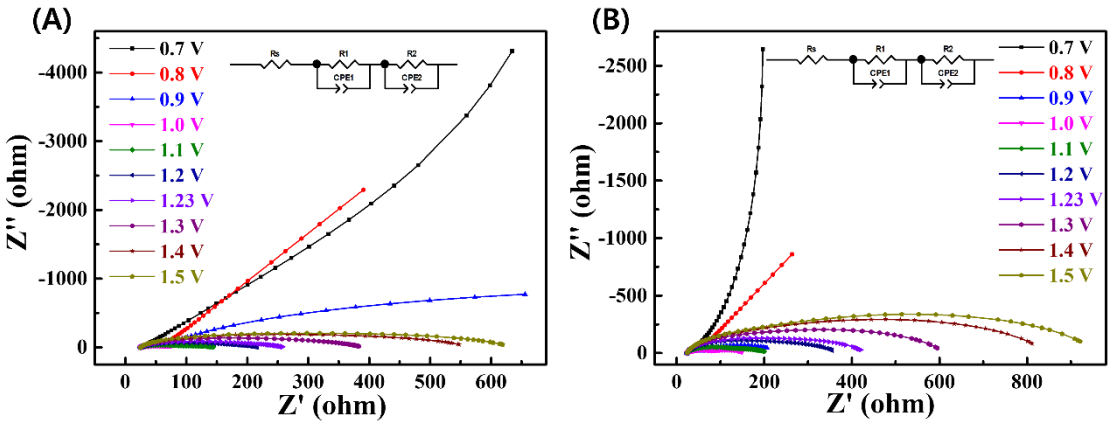

Figure S7. Nyquist plots for (A) Zr/HT and (B) 2:Al-Zr/HT photoanodes obtained at 0.7 – 1.5 V_{RHE} (inset: corresponding equivalent circuit model for EIS fitting).

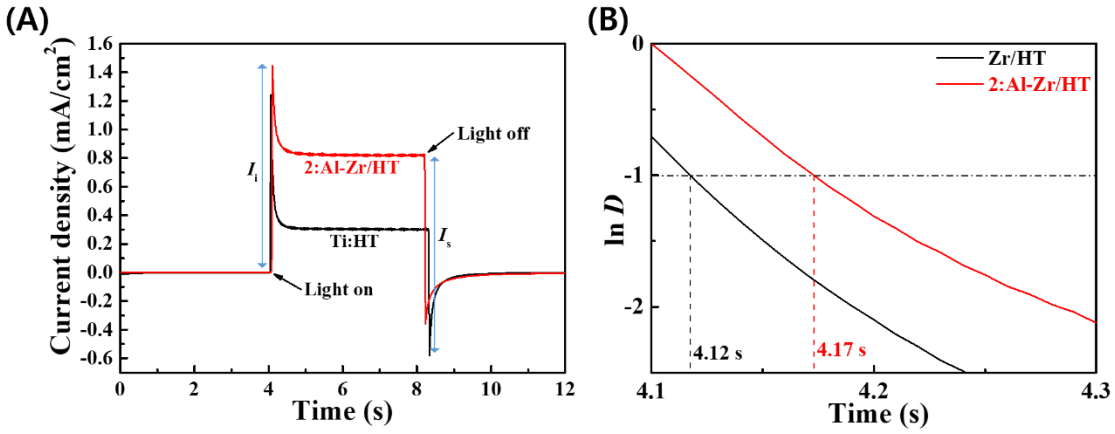

Figure S8. (A) Transient photocurrent response and (B) anodic transient decay time of Zr/HT and 2:Al-Zr/HT photoanode measured at 1.0 V_{RHE} in 1 M NaOH electrolyte under 1-sun illumination condition.

The anodic transient decay time is estimated using the following equation [20]:

$$D = {(I_t - I_s)}/{(I_i - I_s)} \qquad \text{(S8)}$$

where, I_t, I_s and I_i are the time-dependent, steady-state, and initial photocurrent, respectively, as shown in Figure S8A. The transient time constant (τ) is defined as the time when ln D = - 1 in the normalized plots of ln D–t (Figure S8B).

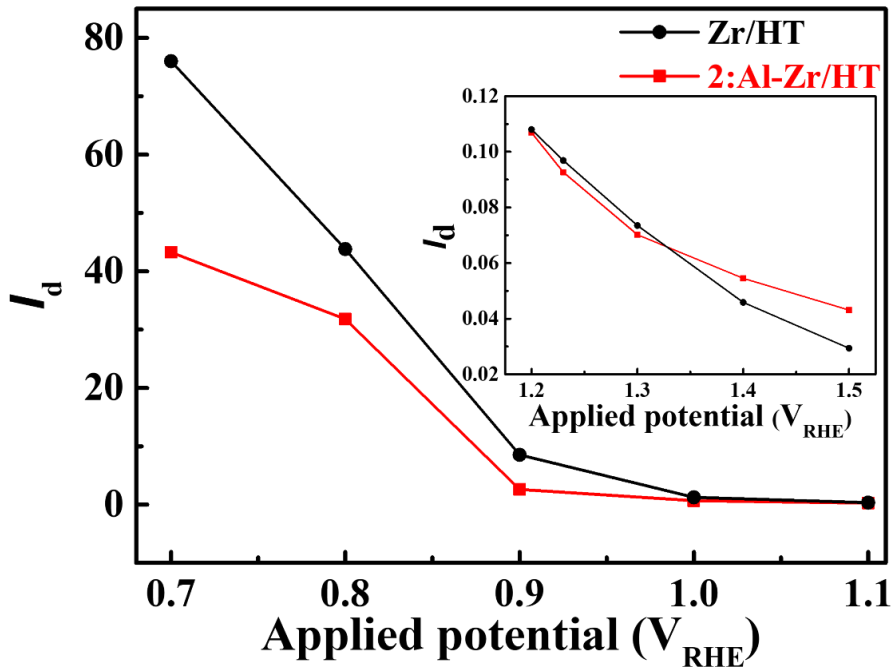

Figure S9. The plots of I_d values vs. Potential for Zr/HT and 2:Al-Zr/HT photoanode. The low I_d indicates fast charge transfer at the interface of electrode/electrolyte.

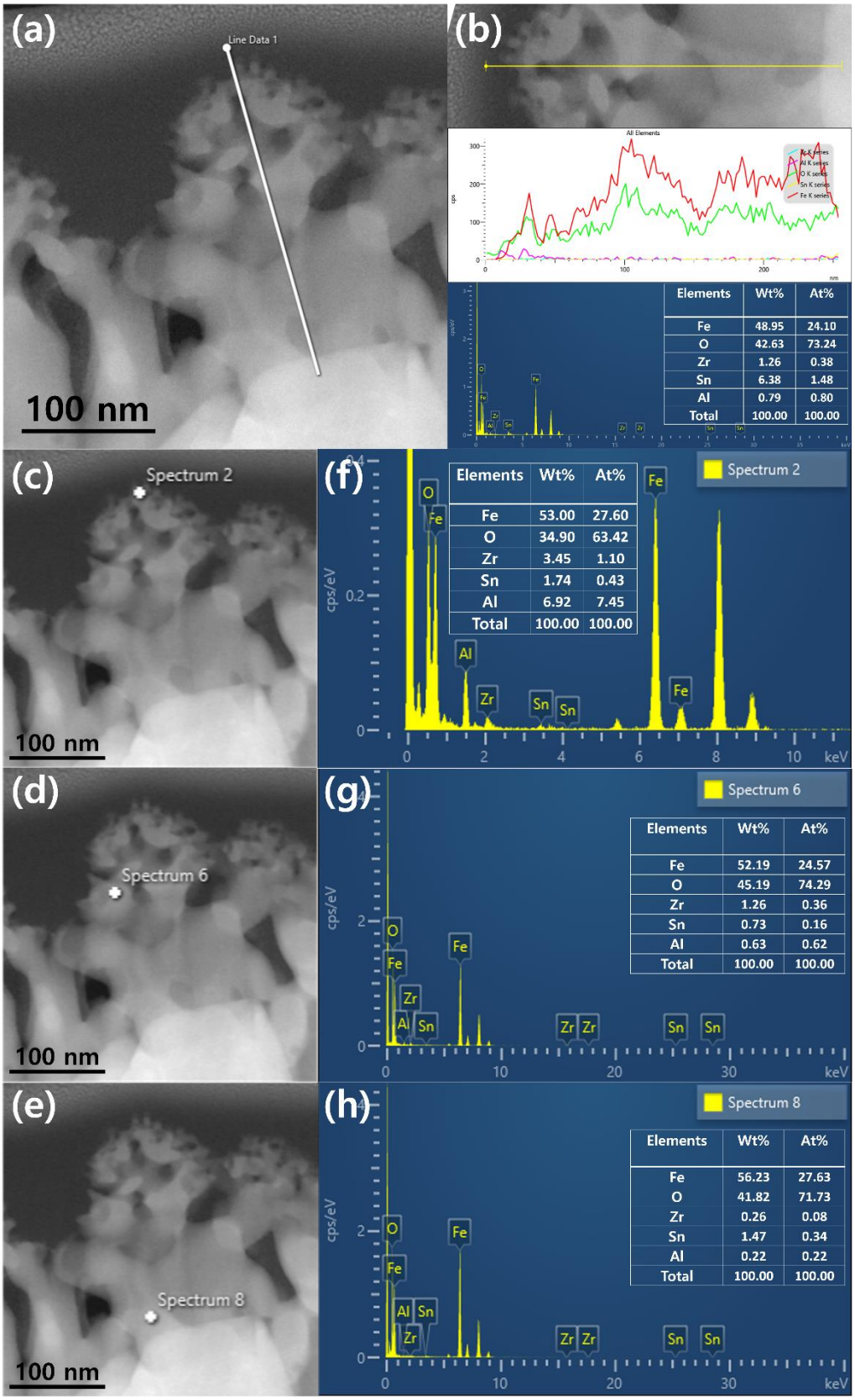

Figure S10. The TEM dark image 2:Al-Zr/HT photoanode indicates the EDS line scan position (a–b), and point scanning (c–h).

Reference

1. M. Saeidi, A. Yourdkhani, S.A.S. Ebrahimi, R. Poursalehi, Candle flame-treatment as an effective strategy to enhance the photoelectrochemical properties of Ti-doped hematite thin films, *J. Mater. Chem. C.* **2020,** *8,* 11950–11961.
2. H. Zhang, Y.K. Kim, H.Y. Jeong, J.S. Lee, A few atomic $FeNbO_4$ overlayers on hematite nanorods: Microwave-induced high temperature phase for efficient photoelectrochemical water splitting, *ACS Catal*. **2018,** *9,* 1289–1297.
3. Y. Lan, Z. Liu, Z. Guo, M. Ruan, Y. Xin, Accelerating the charge separation of $ZnFe_2O_4$ nanorods by Cu-Sn ions gradient doping for efficient photoelectrochemical water splitting, *J. Colloid Interface Sci.* **2019**, *552*, 111–121.
4. Kleiman-Shwarsctein, A.; Huda, M.N.; Walsh, A.; Yan, Y.; Stucky, G.D.; Hu, Y.S.; Al-Jassim, M.M.; McFarland, E.W. Electrodeposited aluminum-doped α-Fe_2O_3 photoelectrodes: experiment and theory. *Chem. Mater*. **2010**, *22*, 510-517.
5. Zhao, X.; Lu, C.; Li, S.; Chen, Y.; Zhang, G.; Zhang, D.; Feng, K.; Zhong, J. FeFx and Fe_2ZrO_5 Co-modified hematite for highly efficient solar water splitting. *J. Energy Chem*. **2022,** *69*, 414-420.
6. Wang, P.; Wang, S.; Gao, L.; Long, X.; Chai, H.; Li, F.; Wang, Q.; Jin, J. Achieving surface-sealing of hematite nanoarray photoanode with controllable metal–organic frameworks shell for enhanced photoelectrochemical water oxidation. *J. Catal.* **2022**, *413*, 398-406.
7. Wang, T.; Gao, L.; Wang, P.; Long, X.; Chai, H.; Li, F.; Jin, J. Dual-doping in the bulk and the surface to ameliorate the hematite anode for photoelectrochemical water oxidation. *J. Colloid Interface Sci.* **2022,** *624*, 60-69.
8. Dhandole, L.K.; Anushkkaran, P.; Chae, W.S.; Chung, H.S.; Lee, H.H.; Choi, S.H.; Cho, M.; Jang, J.S. Efficient charge transfers in hematite photoanode integrated by fluorine and zirconia co-doping for photoelectrochemical water splitting. *Chem. Eng. J*. **2022,** *446*, 136957.
9. Sun, Z.; Fang, G.; Li, J.; Mo, J.; He, X.; Wang, X.; Yu, Z. Preparation of (Ti, Zr) co-doped hematite photoanode for enhanced photoelectrochemical water splitting. *Chem. Phys. Lett.* **2020**, *754*, 137736.
10. Chen, D.; Liu, Z.; Dua-axial gradient doping (Zr and Sn) on hematite for promoting charge separation in photoelectrochemical water splitting. *ChemSusChem* **2018**, *11*, 3438-3448.
11. Hwang, J.B.; Dhandole, L.K.; Anushkkaran, P.; Chae, W.S.; Choi, S.H.; Lee, H.H.; Jang, J.S. Microwave-assisted surface attachment of aluminium ions on in situ diluted titanium-doped hematite photoanodes for efficient photoelectrochemical water-splitting. *Sustain. Energy Fuels* **2022**, *6*, 3056-3067.
12. Kang, K.; Zhang, H.; Kim, J.H.; Byun, W.J.; Lee, J.S. An in situ fluorine and ex situ titanium two-step co-doping strategy for efficient solar water splitting by hematite photoanodes. *Nanoscale Adv*. **2022**, *4,* 1659-1667.
13. Zhu, Q.; Yu, C.; Zhang, X. Ti, Zn co-doped hematite photoanode for solar driven photoelectrochemical water oxidation. *J. Energy Chem.* **2019**, *35*, 30-36.
14. Cherepy, N.J.; Liston, D.B.; Lovejoy, J.A.; Deng, H.; Zhang, J.Z. Ultrafast studies of photoexcited electron dynamics in γ-and α-Fe_2O_3 semiconductor nanoparticles. *J. Phys.*

Chem. B. **1998**, *102*, 770–776.
15. Barroso, M.; Mesa, C.A.; Pendlebury, S.R.; Cowan, A.J.; Hisatomi, T.; Sivula, K.; Grätzel, M.; Klug, D.R.; Durrant, J.R. Dynamics of photogenerated holes in surface modified α-Fe_2O_3 photoanodes for solar water splitting. *PNAS*. **2012**, *109*, 15640–15645.
16. Shen, S.; Guo, P.; Wheeler, D.A.; Jiang, J.; Lindley, S.A.; Kronawitter, C.X.; Zhang, J.Z.; Guo, L.; Mao, S.S. Physical and photoelectrochemical properties of Zr-doped hematite nanorod arrays. *Nanoscale* **2013**, *5*, 9867–9874.
17. Kumar, P. M.; Borse, P.; Rohatgi, V. K.; Bhoraskar, S.V.; Singh, P.; Sastry, M. Synthesis and structural characterization of nanocrystalline aluminium oxide. *Mater. Chem. Phys.* **1994**, *36*, 354–358.
18. Fan, Z.; Xu, Z.; Yan, S.; Zou, Z. Tuning the ion permeability of an Al_2O_3 coating layer on Fe_2O_3 photoanodes for improved photoelectrochemical water oxidation. *J. Mater. Chem. A* **2017**, *5*, 8402–8407.
19. Fang, R.C.; Sun, Q.Q.; Zhou, P.; Yang, W.; Wang, P.F.; Zhang, D.W. High-performance bilayer flexible resistive random access memory based on low-temperature thermal atomic layer deposition. *Nanoscale Res. Lett*. **2013**, *8*, 1–7.
20. Li, J.; Cushing, S.K.; Zheng, P.; Meng, F.; Chu, D.; Wu, N. Plasmon-induced photonic and energy-transfer enhancement of solar water splitting by a hematite nanorod array. *Nat. Commun*. **2013**, *4*, 1–8.